An asymptotic fitting finite element method with exponential mesh refinement for accurate computation of corner eddies in viscous flows

Shapeev, Alexander V.; Lin, Ping

Published in:
SIAM Journal on Scientific Computing

DOI:
10.1137/080719145

Publication date:
2009

Document Version
Publisher's PDF, also known as Version of record

SIAM J. SCI. COMPUT.
Vol. 31, No. 3, pp. 1874–1900

AN ASYMPTOTIC FITTING FINITE ELEMENT METHOD WITH EXPONENTIAL MESH REFINEMENT FOR ACCURATE COMPUTATION OF CORNER EDDIES IN VISCOUS FLOWS*

ALEXANDER V. SHAPEEV† AND PING LIN‡

Abstract. It is well known that any viscous fluid flow near a corner consists of infinite series of eddies with decreasing size and intensity, unless the angle is larger than a certain critical angle [H. K. Moffat, *J. Fluid Mech.*, 18 (1964), pp. 1–18]. The objective of the current work is to simulate such infinite series of eddies occurring in steady flows in domains with corners. The problem is approached by high-order finite element method with exponential mesh refinement near the corners, coupled with analytical asymptotics of the flow near the corners. Such approach allows one to compute position and intensity of the eddies near the corners in addition to the other main features of the flow. The method was tested on the problem of the lid-driven cavity flow as well as on the problem of the backward-facing step flow. The results of computations of the lid-driven cavity problem show that the proposed method computes the central eddy with accuracy comparable to the best of existing methods and is more accurate for computing the corner eddies than the existing methods. The results also indicate that the relative error of finding the eddies' intensity and position decreases uniformly for all the eddies as the mesh is refined (i.e., the relative error in computation of different eddies does not depend on their size).

Key words. finite element method, asymptotic expansion matching, Moffatt eddies near sharp corners

AMS subject classifications. 76D05, 76M10, 65M60

DOI. 10.1137/080719145

1. Introduction.

The two-dimensional flow of a viscous fluid near the corner between two steady rigid planes was first examined by Moffatt [28]. He established that when the angle between planes is less than a certain critical angle, any flow near the corner consists of infinite series of eddies with decreasing size and intensity as the corner point is approached.

One of the most famous examples of flow in domain with corners is a flow in the lid-driven cavity. The lid-driven cavity problem has become a benchmark problem for researchers to test the performance of numerical methods designed for computation of viscous fluid flow. Particularly, among other criteria, the researchers examine the accuracy of their methods based on how accurately they can compute the corner eddies. However, in the previous works only a few eddies were computed (maximum four corner eddies [4, 18] for certain Reynolds numbers). In addition, the accuracy of finding intensity and position of the smaller eddies was less than the accuracy for the larger eddies.

The only attempt known to the authors to compute a large number of corner eddies for the lid-driven cavity problem is the work of Gustafson and Leben [25]. They

*Received by the editors March 24, 2008; accepted for publication (in revised form) December 1, 2008; published electronically March 13, 2009. This research is partially supported by the Singapore Academic Research Funds R-146-000-064-112 and R-146-000-099-112.

http://www.siam.org/journals/sisc/31-3/71914.html

†Department of Mathematics, National University of Singapore, 2, Science Drive 2, Singapore 117543. Current address: Lavrentyev Institute of Hydrodynamics SB RAS, 15 Lavrentyev pr., Novosibirsk, Russia, 630090 (alexander@shapeev.com).

‡Department of Mathematics, National University of Singapore, 2, Science Drive 2, Singapore 117543. Current address: Division of Mathematics, University of Dundee, 23 Perth Road, Dundee, Scotland DD1 4HN, UK (plin@maths.dundee.ac.uk).

computed a large number of eddies (up to ten) for the Stokes flow (Re = 0) on a sequence of subregions contracting to a corner point, setting the boundary conditions for the smaller subregion by interpolation of solution on the larger subregions. However, their method starts with a large error due to initial grid being coarse, and this error does not decrease when interpolating the solution onto the finer grids. Gustafson and Leben pointed out that "Global interaction with the coarser grids is needed to improve the solutions on all levels." However, no works implementing this are known to the authors of the present work.

Flows near the corner between two steady rigid planes have a weak singularity near the corner: Flows of such type decay at a rate proportional to some power of distance to the corner point. Therefore, the derivatives of sufficiently high degree are not bounded in the neighborhood of the corner point. Because of these properties, special treatment of singularities might be required to solve numerically the problem with corner singularities.

It has been noticed that the solutions in domains with corners for problems of fluid mechanics as well as in other disciplines have singularities which cause a slow convergence rate (or sometimes divergence) of numerical methods. It has been found out that local mesh refinement near corners and use of analytical formulas of asymptotic solution near corners produce better results for problems with corner singularities. Some of the popular techniques to overcome slow convergence are as follows: singular function method [19, 35], singular complement method [2], dual singular function method [6, 7, 10, 11], introduction of analytical constraints to finite element formulation [33], truncation of corners and introduction of Dirichlet-to-Neumann boundary conditions for domains with truncated corners [21], and other methods based on the similar ideas [26, 34]. Also, various methods based solely on mesh refinement (without using asymptotic expansion of the solution) were developed (see, for example, [1, 3, 14, 30, 31]). Mesh refinement for biharmonic boundary-value problems is discussed in [5]. Most of the works devoted to solving problems with singularities at corners, however, either used unrefined mesh [2, 6, 10, 11], or algebraically refined mesh [1, 3, 14, 21, 30, 31].

The aim of this paper is not simply to obtain better results, but to develop a systematic method that can accurately compute position and intensity of infinite series of eddies in addition to computing the other main features of flow in domains with corners. The proposed method is based on the techniques developed for problems with corner singularities, namely: Local mesh refinement near the corners and use of asymptotic solution. The proposed local mesh refinement is exponential in the polar radius r and uniform in the polar angle θ. A standard C^1-continuous finite element discretization (namely, Argyris elements) was applied to the stream function equation. Theoretical and numerical justification of the proposed method is provided. The proposed method was applied to the lid-driven cavity problem as well as to the backward-facing step problem. The computations indicate that the proposed method allows one to accurately compute the infinite series of eddies, with the relative error of finding intensity and position of different eddies being independent of their size. The words "asymptotic fitting" in the name of our method are motivated by the long-existing exponential fitting method which is designed to uniformly resolve exponential layers in singular perturbation problems (see a collection of such methods in [32]).

In this paper, by computing an infinite series of eddies we mean producing an approximate formula of computing eddies' intensity and position depending on the number of the eddy. However, strictly speaking, the number of eddies we can practically compute is limited by floating point arithmetic.

The structure of the paper is as follows. In section 2 we give the problem formulation and discuss the properties of flows with infinite series of eddies. In section 3 we describe the proposed method for computing the infinite series of eddies. In section 4 we present and discuss the results of computation of two problems: The lid-driven cavity problem and the backward-facing step problem. Finally, the concluding remarks are given in section 5.

2. Problem formulation. The problem of viscous fluid flow in domain Ω is governed by the Navier–Stokes equations, which in 2D can be written in the form of a single equation for the stream function φ:

$$\Delta\Delta\varphi + \mathrm{Re}\left(\frac{\partial\Delta\varphi}{\partial x}\frac{\partial\varphi}{\partial y} - \frac{\partial\Delta\varphi}{\partial y}\frac{\partial\varphi}{\partial x}\right) = 0, \quad (x,y)\in\Omega, \tag{2.1}$$

where Re is the Reynolds number. This equation will be referred to as the stream function formulation of the Navier–Stokes equations. For simplicity, we consider only the Dirichlet boundary conditions, which cover nonslip, moving wall, and inlet/outlet boundary conditions:

$$\varphi|_{\partial\Omega} = \varphi_0, \quad \left.\frac{\partial\varphi}{\partial n}\right|_{\partial\Omega} = \varphi_1, \quad (x,y)\in\partial\Omega, \tag{2.2}$$

where $\partial\Omega$ is the boundary of Ω, and $\frac{\partial}{\partial n}$ is the outward normal derivative on $\partial\Omega$. The variational formulation of (2.1) and (2.2) is: Find $\varphi\in H^2(\Omega)$ such that

$$\begin{cases} \mathrm{Re}\displaystyle\int_\Omega \left(\frac{\partial\varphi}{\partial x}\frac{\partial\varphi}{\partial y}\left(\frac{\partial^2\psi}{\partial x^2} - \frac{\partial^2\psi}{\partial y^2}\right) - \left(\left(\frac{\partial\varphi}{\partial x}\right)^2 - \left(\frac{\partial\varphi}{\partial y}\right)^2\right)\frac{\partial^2\psi}{\partial x\partial y}\right)dxdy \\ \quad + \displaystyle\int_\Omega \Delta\varphi\Delta\psi dxdy = 0 \quad \left(\forall\psi\in H_0^2(\Omega)\right), \\ \varphi|_{\partial\Omega} = \varphi_0, \quad \left.\dfrac{\partial\varphi}{\partial n}\right|_{\partial\Omega} = \varphi_1. \end{cases} \tag{2.3}$$

The structure of the flow depends on the problem under consideration. Our particular interest is the structure of the flow in the vicinity of the corners. As was found by Moffatt, any flow near the corner with angle smaller than the critical one consists of a series of eddies with decreasing size and intensity as the corner point is approached [28]. The first (i.e., largest) eddies can be affected by the flow far from the corner as well as by the nonlinear forces. However, such impact on the smaller eddies can be neglected, and therefore their behavior is expected to be close to the behavior of the family of asymptotic solutions. To summarize, the flow domain consists of

1. the part without the corner eddies,
2. the part with the relatively large corner eddies that might not be well described by the asymptotic solution due to the impact of the flow far from the corner as well as the impact of the nonlinear forces, and finally,
3. the part with the relatively small eddies that are well described by the asymptotic solution.

To compute such structure of the flow, the computational method should have specific properties. Namely, in the first part of the domain the mesh can be uniform (unless there are other singular features of the solution that are of interest); in the second part the mesh should be refined in such a way that all the eddies are represented with approximately the same number of triangles in order to compute the eddies

uniformly accurately; in the third part the asymptotic solution itself can be used as a discretization.

To derive the asymptotics for the solution near the corner, following the work of Moffatt [28], we can neglect the nonlinear terms because the velocity near the corner between two rigid planes tends to zero. The polar coordinates, with the corner point as the origin, can be separated in (2.1), and hence the main term in the asymptotic solution can be found as the real part of the following complex-valued function:

$$\varphi = Cr^{\lambda} f_{\lambda}(\theta), \tag{2.4}$$

where

$$f_{\lambda}(\theta) = d_1 \cos(\lambda\theta) + d_2 \sin(\lambda\theta) + d_3 \cos((\lambda-2)\theta) + d_4 \sin((\lambda-2)\theta).$$

Parameters d_1, d_2, d_3, and d_4 are found from the nonslip boundary conditions and λ is defined to satisfy the Stokes equation. Particularly, for the case of right angle

$$f_{\lambda}(\theta) = \sin\theta \, \sin\left((\pi/2-\theta)\ (\lambda-1)\right) + \sin\left(\pi/2-\theta\right) \sin\left(\theta\ (\lambda-1)\right), \tag{2.5}$$

and $\lambda \approx 3.74 + 1.12i$. See [8, 27] for a rigorous mathematical theory on asymptotic expansion of the biharmonic equation near a corner.

This asymptotic solution allows one to find the asymptotic ratio of eddies' position and intensity, which are defined as position and value of stream function φ at a local extrema. However, absolute position and intensity of eddies depend on the complex-valued constant C which depends on the particular problem. This constant can be found numerically for each corner of the domain. By finding the constant C, we can compute position and intensity of the infinite series of eddies in each corner of the domain in the following way.

We find position (θ_k, r_k) and intensity (φ_k) of the eddies as local extrema of the real part of φ in (2.4):

$$\frac{\partial \Re(\varphi)}{\partial r} = 0, \quad \frac{\partial \Re(\varphi)}{\partial \theta} = 0,$$

or after substituting (2.4):

$$\Re\left(C\lambda r^{\lambda-1} f_{\lambda}(\theta)\right) = 0, \tag{2.6}$$

$$\Re\left(Cr^{\lambda} \frac{d}{d\theta} f_{\lambda}(\theta)\right) = 0. \tag{2.7}$$

Here $\Re$ denotes the real part of a complex number. Simple analysis shows that these equations can be satisfied only on the bisector $\theta = \pi/4$, in which case (2.7) is satisfied automatically. Hence r can be found by substituting $\theta = \pi/4$ into (2.6):

$$\Re\left(r^{\lambda-1}\, C\lambda f_{\lambda}(\pi/4)\right) = 0.$$

Taking into account that $f_{\lambda}(\pi/4) \neq 0$ and

$$r^{\lambda-1} = e^{(\lambda-1)\ln r} = e^{(\Re(\lambda)-1)\ln r}(\cos\left(\Im(\lambda)\ln r\right) + i\sin\left(\Im(\lambda)\ln r\right)),$$

where $\Im$ is the imaginary part of a complex number, we can write position (r_k, θ_k) of the eddies as

$$\theta_k = \frac{\pi}{4}, \quad r_k = e^{\Im(\lambda)\left(-\pi k + \operatorname{arccot}\left(\arg\left(C\lambda f_{\lambda}\left(\frac{\pi}{4}\right)\right)\right)\right)}, \tag{2.8}$$

where the eddies are numbered with $k = k_0, k_0 + 1, \ldots$ in order of decreasing size. Finally, to find intensity of the eddies φ_k we substitute (r_k, θ_k) into (2.4):

$$\varphi_k = r_k^{\Re(\lambda)} \left|C\lambda f(\pi/4)\right| \Im\left(\frac{1}{\lambda}\right) = e^{\Re(\lambda)\Im(\lambda)\left(-\pi k + \operatorname{arccot}\left(\arg\left(C\lambda f_\lambda\left(\frac{\pi}{4}\right)\right)\right)\right)} \left|C\lambda f\left(\frac{\pi}{4}\right)\right| \Im\left(\frac{1}{\lambda}\right). \tag{2.9}$$

In practice, we can find the constant C only approximately. It means that in computations, there will be some error in eddies' intensity and positions computed by (2.8) and (2.9) due to the error in C. However, we can deduce from formulas (2.8) and (2.9) that the relative error of computing the eddies does not depend on k, because k appears in the formula only as some factor which does not involve C. Indeed, if we denote $\tilde{C}$ to be the approximation to C with the relative error $\delta C = \frac{\tilde{C}-C}{C}$, and $\tilde{\theta}_k$, $\tilde{r}_k$, $\tilde{\varphi}_k$ to be approximate position and intensity of the eddies, computed by (2.8) and (2.9) with approximate $\tilde{C}$ instead of exact C, then the relative error of eddies' position and intensity will be the following:

$$\begin{cases} \delta\theta_k = 0, \\ \delta r_k = e^{\Im(\lambda)\left(\operatorname{arccot}\left(\arg\left(\tilde{C}\lambda f_\lambda\left(\frac{\pi}{4}\right)\right)\right) - \operatorname{arccot}\left(\arg\left(C\lambda f_\lambda\left(\frac{\pi}{4}\right)\right)\right)\right)} - 1 = -\Im(\delta C) + O(\delta C)^2, \\ \delta\varphi_k = \dfrac{|\tilde{C}|}{C} e^{\Re(\lambda)\Im(\lambda)\left(\operatorname{arccot}\left(\arg\left(\tilde{C}\lambda f_\lambda\left(\frac{\pi}{4}\right)\right)\right) - \operatorname{arccot}\left(\arg\left(C\lambda f_\lambda\left(\frac{\pi}{4}\right)\right)\right)\right)} - 1 \\ \qquad = \Re(\delta C) - \Im(\delta C)\Re(\lambda)\Im(\lambda) + O(\delta C)^2. \end{cases} \tag{2.10}$$

The formulas (2.10) are derived by substitution $C = \tilde{C} + \delta C$, $\theta_k = \tilde{\theta}_k + \delta\theta_k$, $r_k = \tilde{r}_k + \delta r_k$, and $\varphi_k = \tilde{\varphi}_k + \delta\varphi_k$ into (2.8) and (2.9), and eliminating $\tilde{\theta}_k$, $\tilde{r}_k$, and $\tilde{\varphi}_k$ computed by formulas (2.8) and (2.9) with exact C substituted by approximate $\tilde{C}$. The formulas (2.10) present the major term in Taylor expansion of $\delta\theta_k$, δr_k, $\delta\varphi_k$ with respect to δC. Thus, as we can see, the relative error of different eddies depends only on C (particularly, it does not depend on k) and converges to zero as $\delta C \to 0$.

By approximately finding the constant C, it is possible to have the uniform relative error for all the eddies in a numerical method. However, to our knowledge, no existing methods can attain it. Our method introduced in this paper attains the uniform relative error, which is numerically demonstrated in section 4. Particularly, we will observe that the relative error of finding eddies' intensity and position decreases uniformly for all the eddies as the mesh is refined (i.e., the relative error in computation of different eddies does not depend on their size).

3. Computational method. The discretization of the stream function formulation of the Navier–Stokes equations in variational form (2.3) is based on Argyris elements. In order to compute the corner eddies uniformly accurately, a special mesh and basis functions are constructed near the corners. The nonlinear system of algebraic equations resulted from the discretization of (2.3) is solved using Newton's iteration. The linearized system of algebraic equations is solved by the unsymmetric multifrontal method [16, 17] implemented in UMFPACK software package.

Analysis of the literature dedicated to numerical solution of the lid-driven cavity problem indicates that the methods with nonuniform mesh refinement near the boundaries generally produce more accurate results for the corner eddies, though the primary eddy might be computed as accurately as when using uniform meshes. However, in the literature on the lid-driven cavity problem, the mesh refinement function (grading function) is usually fixed to be piecewise polynomial in each Cartesian coordinate, and it is usually not discussed what is the optimal mesh refinement to resolve

the eddy structure. A number of works [1, 3, 14, 30, 31] used algebraic mesh refinement near corners in the other applications. Algebraic mesh refinement is used to preserve the convergence rate of the solution globally (the convergence rate is otherwise reduced due to corner singularities). However, it is usually not discussed what mesh refinement should be used in order to accurately resolve singularities near corners.

To accurately resolve the eddy structure near a corner, one should compute a complex-valued constant C in the asymptotic solution (2.4). Having found the constant C, one can compute the eddy structure near the corner by formulas (2.8) and (2.9).

Finding constants of asymptotic expansion of the solution near corners has important applications in elasticity and fracture mechanics, as well as in electromagnetism. A number of methods have been proposed for computing the constants of asymptotic expansion (called "stress intensity factors" in elasticity). Most of the works considered only linear problems [2, 7, 10, 11, 19, 21, 26, 33, 35]. Blum [6] discussed application of dual singular function method to semilinear biharmonic equations, such as the Navier–Stokes equations or the von Kármán equations, however, presenting the numerical results only for linear problems. Shi et al. proposed a method that combines asymptotics of the solution and local mesh refinement near a corner for solution of the Navier–Stokes equations [34]. The authors of [34] mentioned using a local block mesh refinement, which seems to be equivalent to algebraic mesh refinement.

Hawa and Rusak used both exponential local grid refinement and asymptotics of the solution for their finite difference method applied to the backward-facing step flow [26]. They reported improvement of accuracy of the solution near the expansion corner. However, the grid was refined in such a way that if we fix a small region $r_1 < r < r_2$ near the corner, the number of grid nodes in this region will be the same for the coarse and for the refined grid.

In the proposed method, we use the exponential mesh refinement near the corners. With exponential mesh refinement, each corner eddy large enough to be resolved on a given mesh has approximately equal number of triangles for its representation. The mesh is refined in both radial and angular directions, so that the number of triangles for representation of corner eddies is increased with each mesh refinement, thus increasing accuracy of computing the corner eddies. In addition, we assume that in the triangle adjacent to the corner, size and intensity of the eddies are small enough so that the flow in that triangle is well represented by the analytical asymptotics.

The ideas of using such grid refinement are contained in the work of Gustafson and Leben [25]. Their computational procedure consisted in computing the solution on a uniform grid in the whole domain and then projecting it on finer local grids near the corner. The solution on a uniform grid contains a large error originating from corner singularity, and this error does not decrease when the solution is projected on the finer grids. Gustafson and Leben pointed out that "Global interaction with the coarser grids is needed to improve the solutions on all levels." A method with such global interaction, augmented with fitting the numerical solution to the exact asymptotics, would in a certain way be equivalent to the method proposed in the present work. However, no works implementing such kind of methods are known to the authors of the present work.

To construct a mesh, the domain is decomposed into several subdomains according to the structure of the flow: The main subdomain without the corner eddies, the near-corner subdomains with the relatively large corner eddies, and the corner subdomains with the small eddies. Thus, the domain is decomposed into $1 + 2N_c$ subdomains, where N_c is the number of corners between rigid walls (the corners ad-

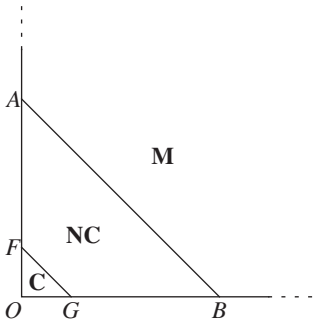

FIG. 3.1. *Domain decomposition near the corner.*

jacent to inlets/outlets are not counted since infinite series of eddies do not occur there). A typical domain decomposition near a corner is shown in Figure 3.1. There is one main subdomain (tagged with "M" in Figure 3.1), one near-corner subdomain per each corner between rigid walls (tagged with "NC" in Figure 3.1), and one corner subdomain per each corner between rigid walls (tagged with "C" in Figure 3.1).

In the present method, the constant C of the asymptotic solution (2.4) near the corners is embedded into the finite element discretization: Its real and imaginary parts are found simply as the coefficients of the expansion of the numerical solution in the finite element basis.

Apart from infinite series of eddies, there can be other singularities in the flow at the corners. For example, in the lid-driven cavity problem, there are singularities at the corners between the moving lid and the side walls (see [24] for details):

$$\varphi = \frac{2r}{\pi^2 - 4}\left((\pi - 2\theta)\sin(\theta) - \pi\theta\cos(\theta)\right) + O(r^2), \tag{3.1}$$

where $r > 0$ and $0 < \theta < \pi/2$ are polar coordinates, chosen so that the origin is in the upper corner of the cavity and $\theta = \pi/2$ corresponds to the cavity lid. In the backward-facing step problem, there is a singularity at the backward-facing corner (see [26])

$$\varphi = C_1 f_{\lambda_1}(\theta) r^{\lambda_1} + C_2 f_{\lambda_2}(\theta) r^{\lambda_2} + O(r^{\lambda_3}), \tag{3.2}$$

where $\lambda_1 \approx 1.54$, $\lambda_2 \approx 1.91$, and $\lambda_3 \approx 2.63 + 0.23i$. It was previously found out that a special treatment of these singularities can produce better results [9, 26]. The technique we use to treat the corner singularities is similar to the technique we use to compute the corner eddies. Namely, we perform the same mesh refinement and we match the asymptotic expansion (3.1) or (3.2) at the corner triangle with the solution at the near-corner subdomain.

The organization of the rest of the section follows the proposed structure of the domain. First, the discretization in the main subdomain is specified (subsection 3.1). Second, the discretization in the near-corner subdomains is described (subsection 3.2). Last, the discretization in the corner subdomains is derived (subsection 3.3).

3.1. Discretization in the main subdomain. The discretization of the stream function formulation of the Navier–Stokes equations in variational form (2.3) in the main subdomain is done on the uniform mesh and is based on Argyris elements, which are the standard C^1-continuous, P_5 finite elements on a triangular mesh:

$$V_h = \left\{\varphi :\ \varphi \text{ is } C^1\text{-continuous}, \varphi \in P_5(T) \text{ for each triangle T}\right\}.$$

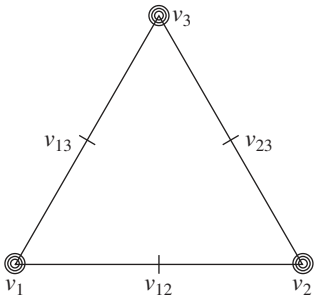

FIG. 3.2. *Argyris elements.*

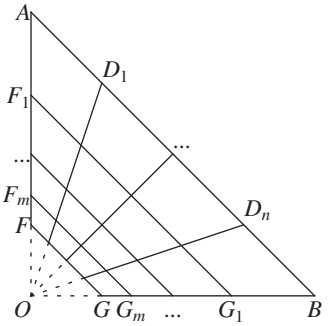

FIG. 3.3. *Trapezia splitting of the near-corner subdomain.*

Argyris elements are schematically shown in Figure 3.2. The basis functions for such finite element discretization are determined by 21 degrees of freedom: Six degrees of freedom at each vertex of the triangle corresponding to the values of φ and its first and second derivatives, and one degree of freedom corresponding to the normal derivative at the middle point of each edge [15, p. 44]:

$$\varphi(v_i),\ \frac{\partial\varphi}{\partial x}(v_i),\ \frac{\partial\varphi}{\partial y}(v_i),\ \frac{\partial^2\varphi}{\partial x^2}(v_i),\ \frac{\partial^2\varphi}{\partial x\partial y}(v_i),\ \frac{\partial^2\varphi}{\partial y^2}(v_i),\quad (i=1,2,3);$$
$$\frac{\partial\varphi}{\partial n}(v_{ij}),\quad (i,j=1,2,3,\ i<j).$$

Here v_i are the vertices of the triangle and v_{ij} are the midpoints of the edges (Figure 3.2).

3.2. Discretization in the near-corner subdomains. The discretization of (2.3) in the near-corner subdomain (trapezium $ABGF$ in Figure 3.1) is also based on Argyris elements and is done on the exponentially graded mesh. The mesh is chosen to be conforming with the mesh in the main subdomain, and therefore no additional techniques are involved to couple the solutions in these two subdomains.

To construct the mesh, the region $ABGF$ is split into the smaller trapezia (Figure 3.3) by introducing a series of line segments parallel to AB (denoted as F_1G_1, ..., F_mG_m on the Figure 3.3) and another series of segments of the lines whose extensions cross at the corner point O (these lines are denoted as OD_1, ..., OD_n in Figure 3.3). Position of the lines crossing at O is induced by the triangulation in the main subdomain: These lines contain the nodes of the triangulation on the line segment AB.

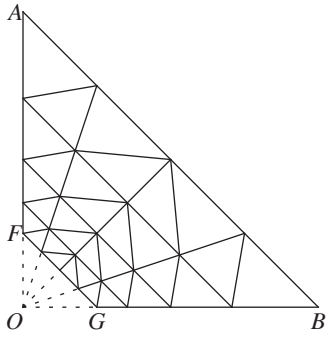

FIG. 3.4. *Triangular mesh of the near-corner subdomain.*

The distances between the lines parallel to AB are chosen to satisfy the exponential refinement property: The ratio of lengths of the adjacent intervals on AF and BG is constant:

$$\frac{F_2F_1}{F_1A} = \frac{F_3F_2}{F_2F_1} = \ldots = \frac{F_mF_{m-1}}{F_{m-1}F_{m-2}} = \frac{FF_m}{F_mF_{m-1}} = k.$$
$$\frac{G_2G_1}{G_1B} = \frac{G_3G_2}{G_2G_1} = \ldots = \frac{G_mG_{m-1}}{G_{m-1}G_{m-2}} = \frac{GG_m}{G_mG_{m-1}} = k.$$

The constant k is chosen as

$$k = 2^{-1/n} \tag{3.3}$$

to agree with the mesh in the main subdomain and to avoid triangles with small angles. Here m is the number of subdivisions of GB (hereinafter referred as the number of radial subdivisions), and n is the number of subdivisions of AB (hereinafter referred as the number of angular subdivisions).

Finally, after splitting the near-corner subdomain into trapezia, each trapezium is divided into two triangles avoiding obtuse triangles (Figure 3.4). These triangles form the triangulation in the near-corner subdomain.

3.3. Discretization in the corner subdomains. We assume that in the corner subdomain (triangle OFG in Figure 3.1), the asymptotics (2.5) give a sufficiently accurate approximation to the exact solution. Therefore, the solution basis in the corner triangle OFG is chosen to be a set of only two functions, namely real and imaginary part of the function $r^\lambda f_\lambda(\theta)$ in (2.5):

$$V_h(\triangle_{OFG}) = \{\varphi_1|_{\triangle_{OFG}}, \varphi_2|_{\triangle_{OFG}}\} = \left\{ \Re\left(r^\lambda f_\lambda\right)\big|_{\triangle_{OFG}}, \Im\left(r^\lambda f_\lambda\right)\big|_{\triangle_{OFG}} \right\}. \tag{3.4}$$

In this case finding the constant C of asymptotics (2.4) is equivalent to finding the coefficients of expansion of the numerical solution in the basis (3.4):

$$\varphi = \Re\left(Cr^\lambda f_\lambda\right) = \Re(C)\Re\left(r^\lambda f_\lambda\right) - \Im(C)\Im\left(r^\lambda f_\lambda\right) = \Re(C)\varphi_1 - \Im(C)\varphi_2$$

inside $\triangle_{OFG}$.

For the overall finite element discretization to be conforming, the basis functions should be C^1-continuous across the interface FG; that is, the jumps of any basis

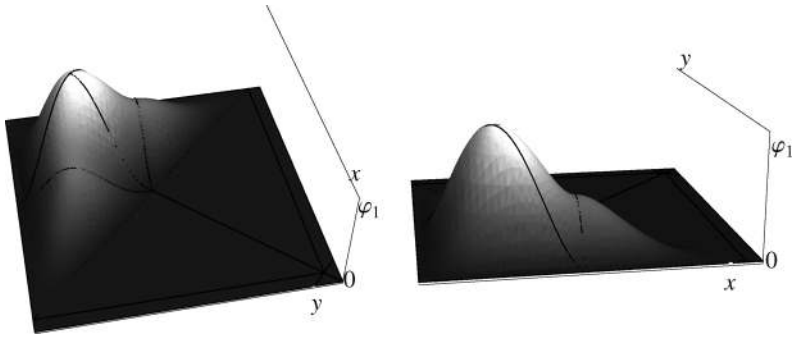

FIG. 3.5. *Basis function near the edge A_1A_2 (1st function, mesh M0).*

function φ_k and its normal derivative should be equal to zero along FG:

$$[\varphi_k]_{FG} = 0, \quad \left[\frac{\partial \varphi_k}{\partial n}\right]_{FG} = 0. \tag{3.5}$$

These conditions, however, cannot be satisfied since the basis functions in $FGBA$ are piecewise polynomials, whereas the basis functions in OFG are not piecewise polynomials. Therefore, we satisfy the interface conditions (3.5) approximately as described below.

If the values of a basis function in OFG were fixed, then the interface conditions (3.5) would be nothing but the Dirichlet conditions at the segment FG. Therefore, we treat the interface conditions (3.5) like the regular Dirichlet boundary conditions: We set the jumps of the function and its first tangential, second tangential, normal, and mixed derivatives to be equal to zero at the mesh points. In addition, we set the jumps of the normal derivative to be equal to zero at the midpoints of the edges. More precisely, if the triangle $v_1v_2v_3$ has the edge v_1v_2 on the interface FG, then the interface conditions are written as

$$\begin{aligned} &[\varphi_k(v_i)]_{FG} = 0, \ \left[\frac{\partial \varphi_k}{\partial s}(v_i)\right]_{FG} = 0, \ \left[\frac{\partial \varphi_k}{\partial n}(v_i)\right]_{FG} = 0, \\ &\left[\frac{\partial^2 \varphi_k}{\partial s^2}(v_i)\right]_{FG} = 0, \ \left[\frac{\partial^2 \varphi_k}{\partial n \partial s}(v_i)\right]_{FG} = 0, \quad (i = 1, 2); \\ &\left[\frac{\partial \varphi_k}{\partial n}(v_{12})\right]_{FG} = 0. \end{aligned} \tag{3.6}$$

The finite element basis constructed in this way approximately satisfies the interface conditions (3.5). Examples of the basis functions are illustrated in Figures 3.5, 3.6, 3.7, and 3.8.

One important remark needs to be made regarding refining the mesh. When refining the mesh by a factor of 2, we expect the error to decrease at most by a factor of 2^6 (since the basis functions are 5th degree polynomials). Then we also should shrink the domain OFG as the mesh is refined in order to reduce the error of representation of the solution with its asymptotics (2.5). This will expand the near-corner domain $FGBA$. The factor of shrinking of the corner domain OFG needs to be chosen in such a way that on the one hand, the error of representation of the solution

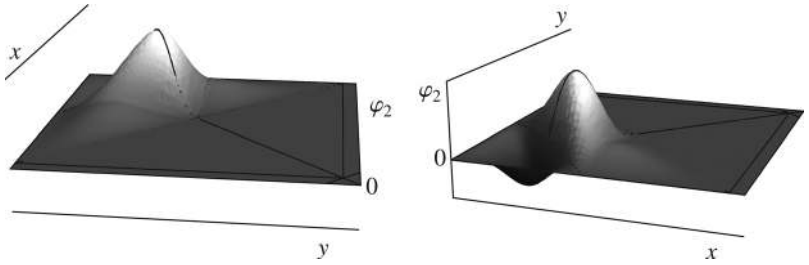

FIG. 3.6. *Basis function near the edge A_1A_2 (2nd function, mesh $M0$).*

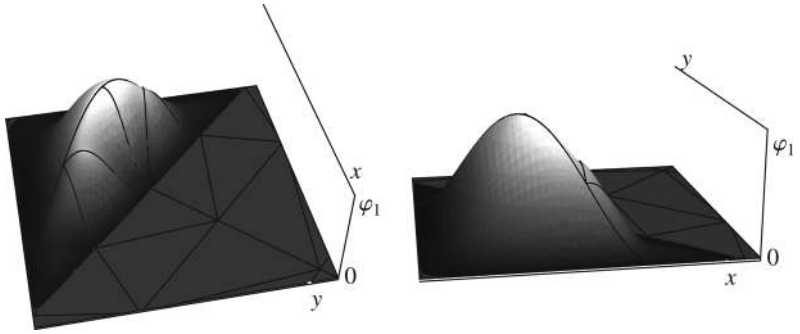

FIG. 3.7. *Basis function near the edge A_1A_2 (1st function, mesh $M1$).*

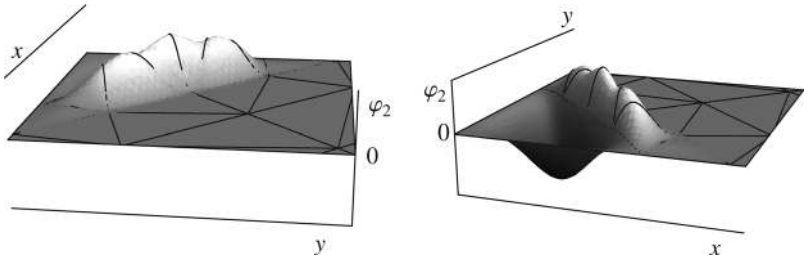

FIG. 3.8. *Basis function near the edge A_1A_2 (2nd function, mesh $M1$).*

with its asymptotics is not dominating, and on the other hand, the number degrees of freedom of the discretization is not too large. From the numerical experiments (see subsection 4.2 for details), it was established that a shrinking factor of 4 is close to the optimal value for computation of the corner eddies. The examples of the meshes in the main and near-corner subdomains for the lid-driven cavity problem are shown in Figure 3.9. The bold lines are the interfaces between subdomains.

4. Results of computations and discussion. The present method was applied to two problems: The lid-driven cavity problem, and the backward-facing step problem. Since the lid-driven cavity problem is the most widely used benchmark problem, the main focus was to compute the infinite series of eddies for the lid-driven cavity flow and compare the data with the results available in the literature (subsection 4.1). Also, different shrinking factors of corner subdomain were tested to confirm that the factor of 4 is close to the optimal value (subsection 4.2). The backward-facing step problem was also computed and compared with the available results (subsection 4.3).

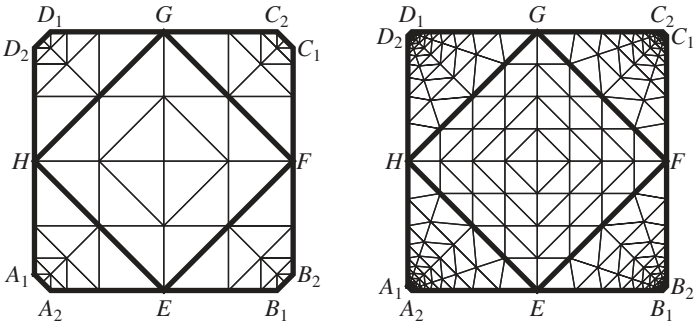

FIG. 3.9. *Main subdomain mesh examples for the lid-driven cavity problem (meshes M0 and M1).*

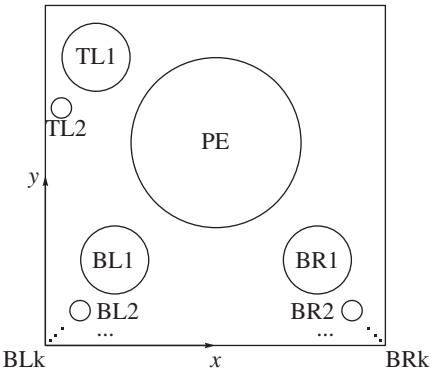

FIG. 4.1. *Schematic structure of the eddies for the lid-driven cavity flow.*

4.1. Lid-driven cavity problem. The lid-driven cavity flow is described by the following boundary-value problem:

$$\begin{cases} \Delta\Delta\varphi + \mathrm{Re}\left(\dfrac{\partial\Delta\varphi}{\partial x}\dfrac{\partial\varphi}{\partial y} - \dfrac{\partial\Delta\varphi}{\partial y}\dfrac{\partial\varphi}{\partial x}\right) = 0, \\ \varphi|_{\partial\Omega} = 0, \\ \left.\dfrac{\partial\varphi}{\partial n}\right|_{\partial\Omega} = u_s, \end{cases}$$

where the domain Ω is the unit square $\Omega = (0,1) \times (0,1)$, and u_s is a tangential velocity on the boundary: $u_s = 1$ for $y = 1$, and $u_s = 0$ otherwise. The general structure of the lid-driven cavity flow is sketched in Figure 4.1. The flow consists of the primary eddy (denoted as PE), a series of bottom left corner eddies (denoted as BL1, BL2, ..., BLk, ...), and a series of bottom right corner eddies (denoted as BR1, BR2, ..., BRk, ...). The eddies are numbered in order of decreasing size. For high Reynolds numbers, the top left eddies (TL1 and TL2) can also appear in the flow. It is generally agreed among researchers that the steady flow is stable for small and moderate Reynolds numbers. However, there has been no agreement regarding the stability of the flow for higher Reynolds numbers (although, we must admit, a number of latest works, see [12] and references therein, suggest that the lid-driven cavity flow looses its stability at $\mathrm{Re} \approx 8000$). We compare our high-Re results with one of the

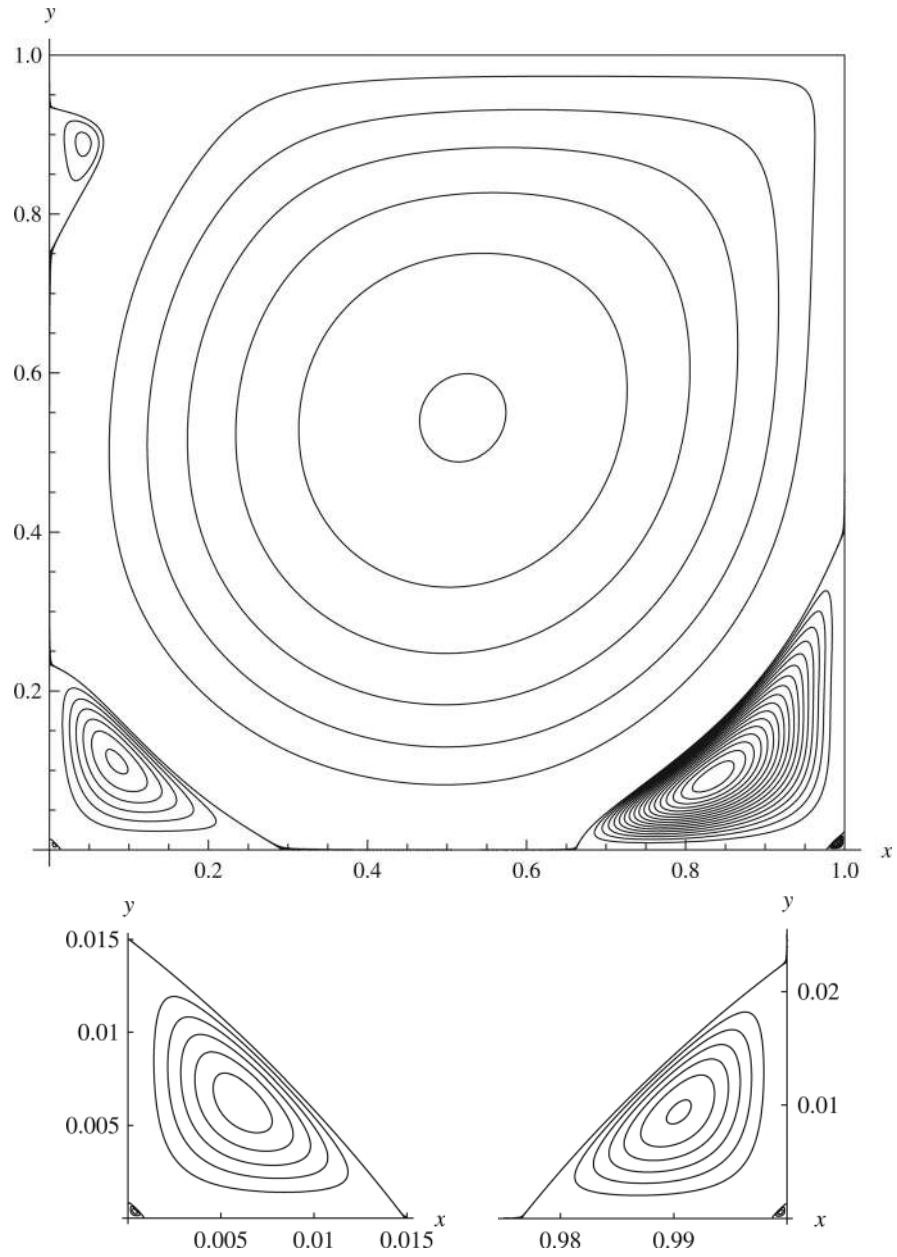

FIG. 4.2. *Streamlines for cavity flow for* Re = 2500.

most accurate results available in the literature, namely with the work of Barragy and Carey [4], who found the numerical solution to be stable up to Re = 12500. Also, we present our results for higher Re in order to illustrate the capability of the present method to compute the infinite series of eddies for higher Re, as well as to make it possible to compare the present results with other works.

The figures with the streamlines of the lid-driven cavity flow for Re = 2500 are presented in Figure 4.2. The upper image contains the eddies PE, TL1, BL1, BR1, and also the small eddies BL2 and BR2. The two lower images contain BL2, BL3 and BR2,

TABLE 4.1
Parameters of meshes used.

Mesh	Triangles	DOF	Reduced DOF	Corner triangle size (OG)	Near-corner radial subdivisions(m)	Near-corner angular subdivisions(n)
M0	68	414	210	0.063	2	1
M1	388	2078	1490	0.016	9	3
M2	2052	10126	8578	0.0039	27	7
M3	10244	48334	44482	0.00098	71	15
M4	49156	226574	217346	0.00024	175	31

BR3, respectively. The images for the smaller eddies are almost not distinguishable from the lower two images and therefore are not presented in the paper.

The lid-driven cavity problem was computed using the method described above. The computations were done on five different meshes, denoted as M0, M1, M2, M3, and M4. The meshes M0 and M1 are shown in Figure 3.9. The parameters such as number of triangles, number of degrees of freedom (DOF), size of a leg of the corner triangle (i.e., length of OG in Figure 3.4), and the number of radial and angular subdivisions of near-corner subdomains (i.e., the numbers m and n introduced in section 3.2) are presented in Table 4.1. The fourth column (reduced DOF) is the number of degrees of freedom after application of the boundary conditions and the matching conditions on the interface between corner and near-corner subdomains. The results on the mesh M0 are substantially underresolved for $\mathrm{Re} \geq 1000$ and therefore are not presented here.

Comparison of the results of the present work on different meshes with the works [9, 13, 18, 20, 22, 29] in the literature was carried out for $\mathrm{Re} = 1000$. The results are presented in Table 4.2 (only the works that produce at least one of the two second corner eddies, BR2 or BL2, were included in the table). The first column of the table indicates the work (the present work or the existing work we compare with). The type of method used and its spatial accuracy are presented in the second column. The abbreviations FE, Sp, and FD denote finite element, spectral, and finite difference method, respectively. The third column indicates the grid (or mesh) used and the number of degrees of freedom in the discretization. The rest of the columns contain intensity (φ) and position (x, y) of the respective eddies.

The best agreement of our results for $\mathrm{Re} = 1000$ is with the results of Botella and Peyret [9], which seem to have the most accurate results for $\mathrm{Re} = 1000$ available in the literature. The absolute difference in stream function at the location of eddies between our work and [9] is less than 10^{-7}. As can be seen from Table 4.2 (rows 5 and 6), the results on the meshes 128×128 and 160×160 are very close to each other and are very close to the results of the present work. The absolute difference in intensity of the primary eddy (PE) is less than 10^{-7} and the difference for BL2 is $6 \cdot 10^{-11}$. However, the relative difference between computations on these two meshes is less than 10^{-6} for the primary eddy, and is approximately 0.01 for BL2. This is the common feature of most of the other methods: The relative accuracy of computation of the corner eddies is less than the accuracy for the primary eddy; the smaller the eddy is, the less the relative accuracy is. On the contrary, for the present method the relative difference between solutions on the meshes M3 and M4 for PE is approximately $1.68 \cdot 10^{-7}$, for BL1 is $1.47 \cdot 10^{-6}$, and for BL2 is $1.49 \cdot 10^{-6}$. This indicates that the proposed method allows one to compute the infinite number of eddies with the relative error of

TABLE 4.2
Comparison of results for $\mathrm{Re} = 1000$.

Work	Method (accur.)	Grid (DOF)		PE	BR1	BL1	BR2	BL2
present	FE (6)	M1 (2078)	φ	-0.118968144	0.001850227	0.0002241393	$-5.419591 \cdot 10^{-8}$	$-6.139487 \cdot 10^{-9}$
			x	0.530196950	0.86028885	0.08276962	0.992144034	0.0048090691
			y	0.566473209	0.11366291	0.077479611	0.007855935	0.0048090691
present	FE (6)	M2 (10126)	φ	-0.118941452	0.001730255	0.0002334403	$-5.041120 \cdot 10^{-8}$	$-6.398213 \cdot 10^{-9}$
			x	0.530791378	0.86404158	0.08327453	0.992324269	0.0048428003
			y	0.565248546	0.11182323	0.078097763	0.007651558	0.0048453434
present	FE (6)	M3 (48334)	φ	-0.118936631	0.001729707	0.0002334532	$-5.039348 \cdot 10^{-8}$	$-6.398563 \cdot 10^{-9}$
			x	0.530790147	0.86404026	0.08327321	0.992324863	0.0048426989
			y	0.565240564	0.11180605	0.078095777	0.007650968	0.0048452431
present	FE (6)	M4 (226574)	φ	-0.118936611	0.001729717	0.0002334529	$-5.039380 \cdot 10^{-8}$	$-6.398554 \cdot 10^{-9}$
			x	0.530790112	0.86404006	0.08327318	0.992324852	0.0048426963
			y	0.565240557	0.11180617	0.078095725	0.007650979	0.0048452406
Botella and Peyret [9]	Sp	128×128 (48644)	φ	-0.1189366	0.00172971	0.0002334528	$-5.03992 \cdot 10^{-8}$	$-6.33255 \cdot 10^{-9}$
			x	0.5308	0.8640	0.0833	0.99232	0.00490
			y	0.5652	0.1118	0.0781	0.00765	0.00482
Botella and Peyret [9]	Sp	160×160 (76164)	φ	-0.1189366	0.00172971	0.0002334528	$-5.03944 \cdot 10^{-8}$	$-6.39800 \cdot 10^{-9}$
			x	0.5308	0.8640	0.0833	0.99232	0.00484
			y	0.5652	0.1118	0.0781	0.00765	0.00484
Erturk et al. [18]	FD (2)	601×601 (722402)	φ	$6 - 0.118781$	0.0017281	0.00023261	$-5.4962 \cdot 10^{-8}$	$-8.4221 \cdot 10^{-9}$
			x	0.5300	0.8633	0.0833	0.9917	0.0050
			y	0.5650	0.1117	0.0783	0.0067	0.0050
Nishida and Satofuka [29]	FD (8)	129×129 (33282)	φ	-0.119004	0.00172787	0.000233520	$-5.48624 \cdot 10^{-8}$	
			x	0.5313	0.8594	0.0859	0.9922	
			y	0.5625	0.1094	0.0781	0.0078	
Ghia et al. [20]	FD (2)	129×129 (33282)	φ	-0.117929	0.00175102	0.000231129	$-9.31929 \cdot 10^{-8}$	
			x	0.5313	0.8594	0.0859	0.9922	
			y	0.5625	0.1094	0.0781	0.0078	
Goyon [22]	FD (2)	129×129 (33282)	φ	-0.1157	0.00163	0.000211	$-8.79 \cdot 10^{-8}$	
			x	0.5312	0.8671	0.0859	0.9921	
			y	0.5625	0.1171	0.0871	0.0078	
Bruneau and Jouron [13]	FD (2)	257×257 (198147)	φ	-0.1163	0.00191	0.000325	$-3.06 \cdot 10^{-8}$	
			x	0.5313	0.8711	0.0859	0.9961	
			y	0.5586	0.1094	0.0820	0.0039	

computation of the corner eddies being essentially independent of their size. We will observe this feature of the proposed method in more detail below.

The results for higher Reynolds numbers were compared with the results of Barragy and Carey [4], which were found to be the most accurate results containing up to the fourth corner eddies. The absolute difference between the present work and [4] in stream function at the location of the eddies is less than 10^{-5}. Intensity and position of some of the eddies for the present computations for the different mesh refinements and the results of Barragy and Carey [4] are presented in Tables 4.3 and 4.4 (for Re = 2500 and Re = 12500, respectively).

Table 4.3 indicates that the present results for Re = 2500 are more accurate for all the eddies than the results of Barragy and Carey. The results for Re = 12500 (Table 4.4) on the mesh M4 seem to be of comparable accuracy for the primary eddy and first three corner eddies (BL1-BL3, BR1-BR3). However, the present method produces better results for the fourth corner eddies (BL4 and BR4) than the method of Barragy and Carey [4]. The deterioration of the accuracy of the present method for high Reynolds numbers is attributed to the uniform mesh being used in the main subdomain in the present method. Barragy and Carey used the graded mesh which might resolve the boundary layers near the walls better.

It is also interesting to examine the relative error of finding intensity and position of different corner eddies depending on the mesh. As can be observed from Table 4.3 (Re = 2500), the difference in eddies' intensity and position between computations on two consecutive meshes M3 and M4 decreases by a large factor (the difference between M3 and M4 is about 30 times smaller than the difference between M2 and M3). This indicates fast convergence of the numerical solution. Hence, we can estimate the error of the solution on M1, M2, and M3 as the difference with the solution on M4. Also, since the difference between the results of Barragy and Carey and the present results on the mesh M4 is much larger than the difference between M3 and M4, we can also estimate the error of Barragy and Carey's solution as the difference between their solution and the present solution on M4. The estimated relative error thus computed for the eddies BL1-BL4 is presented in Table 4.5. As can be seen from Table 4.5, the method of Barragy and Carey (as well as all the methods available in the literature and known to us) produces the relative error which increases for the smaller eddies. On the contrary, the present method allows one to compute the whole infinite series of eddies, and the relative error of finding the eddies' intensity and position decrease uniformly for all the eddies as the mesh is refined. That is, there is a bound on the relative error of finding the eddies' intensity and position; this bound is independent of size and intensity of the particular eddy and decreases as the mesh is refined. This is a distinctive feature of the proposed method, which is a result of appropriate mesh refinement near the corners as well as coupling the approximate solution with the exact asymptotics.

One of the reasons for uniform accuracy of computing corner eddies is the ability of the method to accurately compute the complex-valued constant C in the asymptotic solution (2.4). Table 4.6 presents the computed values of the constant C at the bottom-left and the bottom-right corners. It can be seen that the values of C also converge fast as the mesh is refined. Estimates (2.10) guarantee that once the error of finding C is small, the relative error of position and intensity of the eddies near the corner is also small and is independent of the size of eddy.

Intensity and position of all the eddies present in the flow were computed for Re = 1000, 2500, 5000, 7500, 10000, 12500, 20000, and 25000. The fifth corner eddies (BL5 and BR5) as well as the smaller eddies (sixth, seventh, etc.) were computed for

TABLE 4.3
Comparison of different eddies for Re = 2500 *for different refinements with Barragy and Carey* [4].

PE	φ	x	y
M1	-0.1229531	0.5232264	0.5433070
M2	-0.1214925	0.5197949	0.5439642
M3	-0.1214695	0.5197760	0.5439257
M4	-0.1214690	0.5197769	0.5439244
Barragy&Carey	-0.1214621	0.5188822	0.5434181
BL1	φ	x	y
M1	0.0008589064	0.08486497	0.1124206
M2	0.0009319561	0.08428356	0.1110820
M3	0.0009311176	0.08424130	0.1110051
M4	0.0009311474	0.08424181	0.1110061
Barragy&Carey	0.0009310542	0.08439557	0.1109646
BL2	φ	x	y
M1	$-2.561365 \cdot 10^{-8}$	0.006180366	0.006180366
M2	$-2.813986 \cdot 10^{-8}$	0.006133761	0.006162933
M3	$-2.811056 \cdot 10^{-8}$	0.006129657	0.006158771
M4	$-2.811158 \cdot 10^{-8}$	0.006129716	0.006158831
Barragy&Carey	$-2.809461 \cdot 10^{-8}$	0.006023922	0.006211389
BL3	φ	x	y
M1	$7.062414 \cdot 10^{-13}$	0.0003730432	0.0003730432
M2	$7.758873 \cdot 10^{-13}$	0.0003711063	0.0003711063
M3	$7.750788 \cdot 10^{-13}$	0.0003708568	0.0003708568
M4	$7.751069 \cdot 10^{-13}$	0.0003708612	0.0003708595
Barragy&Carey	$7.595817 \cdot 10^{-13}$	0.0003884944	0.0003884944
BR1	φ	x	y
M1	0.001739386	0.8549169	0.08763599
M2	0.002659379	0.8346474	0.09085711
M3	0.002662588	0.8343961	0.09075836
M4	0.002662432	0.8344014	0.09075692
Barragy&Carey	0.002662249	0.8342324	0.09075121
BR2	φ	x	y
M1	$-6.107748 \cdot 10^{-8}$	0.9922088	0.007791156
M2	$-1.223342 \cdot 10^{-7}$	0.9904728	0.009371962
M3	$-1.226814 \cdot 10^{-7}$	0.9904590	0.009384841
M4	$-1.226678 \cdot 10^{-7}$	0.9904594	0.009384439
Barragy&Carey	$-1.226317 \cdot 10^{-7}$	0.9903702	0.009321324
BR3	φ	x	y
M1	$1.684081 \cdot 10^{-12}$	0.9995297	0.0004702695
M2	$3.372570 \cdot 10^{-12}$	0.9994297	0.0005702880
M3	$3.382143 \cdot 10^{-12}$	0.9994289	0.0005710936
M4	$3.381770 \cdot 10^{-12}$	0.9994289	0.0005710737
Barragy&Carey	$3.366884 \cdot 10^{-12}$	0.9994164	0.0005836428
BR4	φ	x	y
M1	$-4.643492 \cdot 10^{-17}$	0.9999716	0.00002838518
M2	$-9.299140 \cdot 10^{-17}$	0.9999656	0.00003442224
M3	$-9.325535 \cdot 10^{-17}$	0.9999655	0.00003447087
M4	$-9.324506 \cdot 10^{-17}$	0.9999655	0.00003446937
Barragy&Carey	$-5.945803 \cdot 10^{-16}$	0.9999354	0.00006458191
TL1	φ	x	y
M1	0.0002137404	0.03705343	0.8860543
M2	0.0003454710	0.04307404	0.8893125
M3	0.0003434614	0.04300269	0.8893601
M4	0.0003434479	0.04300225	0.8893601
Barragy&Carey	0.0003433099	0.04329169	0.8890354

TABLE 4.4

Comparison of different eddies for Re = 12500 *for different refinements with Barragy and Carey* [4].

PE	φ	x	y
M2	-0.1245284	0.5166685	0.5257130
M3	-0.1223875	0.5109497	0.5288917
M4	-0.1223661	0.5110722	0.5288052
Barragy&Carey	-0.1223584	0.5113304	0.5283202
BL1	φ	x	y
M2	0.001535998	0.05467608	0.1797522
M3	0.001662061	0.05549707	0.1673713
M4	0.001667856	0.05552998	0.1675260
Barragy&Carey	0.001667752	0.05541802	0.1680841
BL2	φ	x	y
M2	$-4.078831 \cdot 10^{-6}$	0.02505156	0.03127547
M3	$-6.622290 \cdot 10^{-6}$	0.02661348	0.03251247
M4	$-6.789915 \cdot 10^{-6}$	0.02678565	0.03269075
Barragy&Carey	$-6.787536 \cdot 10^{-6}$	0.02655169	0.03282161
BL3	φ	x	y
M2	$1.093344 \cdot 10^{-10}$	0.001669520	0.001669520
M3	$1.783343 \cdot 10^{-10}$	0.001759045	0.001760104
M4	$1.828845 \cdot 10^{-10}$	0.001769764	0.001770830
Barragy&Carey	$1.828415 \cdot 10^{-10}$	0.001767080	0.001767080
BL4	φ	x	y
M2	$-3.014661 \cdot 10^{-15}$	0.0001007712	0.0001007712
M3	$-4.917188 \cdot 10^{-15}$	0.0001062069	0.0001062069
M4	$-5.042648 \cdot 10^{-15}$	0.0001068540	0.0001068540
Barragy&Carey	$-4.384933 \cdot 10^{-15}$	0.0001292307	0.00006458191
BR1	φ	x	y
M2	0.002106801	0.7972048	0.05290622
M3	0.003123291	0.7594222	0.05435194
M4	0.003100299	0.7598890	0.05417034
Barragy&Carey	0.003099803	0.7603326	0.05407320
BR2	φ	x	y
M2	-0.00004778892	0.9458347	0.04838712
M3	-0.0002608272	0.9272493	0.08172105
M4	-0.0002559075	0.9273684	0.08114478
Barragy&Carey	-0.0002558322	0.9275135	0.08121944
BR3	φ	x	y
M2	$1.304507 \cdot 10^{-9}$	0.9969275	0.003073027
M3	$7.941352 \cdot 10^{-9}$	0.9951967	0.004828739
M4	$7.759087 \cdot 10^{-9}$	0.9952262	0.004798437
Barragy&Carey	$7.750350 \cdot 10^{-9}$	0.9952875	0.004899706
BR4	φ	x	y
M2	$-3.596902 \cdot 10^{-14}$	0.9998145	0.0001854712
M3	$-2.189624 \cdot 10^{-13}$	0.9997093	0.0002906878
M4	$-2.139370 \cdot 10^{-13}$	0.9997111	0.0002888828
Barragy&Carey	$-2.077842 \cdot 10^{-13}$	0.9996764	0.0002587290
TL1	φ	x	y
M2	0.002659272	0.07126436	0.9117728
M3	0.003017535	0.07416998	0.9103214
M4	0.003006600	0.07406084	0.9104110
Barragy&Carey	0.003006256	0.07407443	0.9100436
TL2	φ	x	y
M2	$-2.128141 \cdot 10^{-7}$	0.003520221	0.8342278
M3	$-1.809690 \cdot 10^{-6}$	0.007213993	0.8302868
M4	$-1.716189 \cdot 10^{-6}$	0.007084863	0.8305045
Barragy&Carey	$-1.712133 \cdot 10^{-6}$	0.007148820	0.8307576

TABLE 4.5
Estimated relative error of finding eddies' intensity for $\mathrm{Re} = 2500$.

	BL1	BL2	BL3	BL4
present, M1	0.077583	0.088858	0.088846	0.088846
present, M2	0.00086856	0.0010060	0.0010069	0.0010069
present, M3	0.000031924	0.000036335	0.000036188	0.000036189
Barragy&Carey	0.00010006	0.00060359	0.020030	-

TABLE 4.6
Computed constant C *at the bottom-left and the bottom-right corner for* $\mathrm{Re} = 2500$.

	C at the bottom-left corner	C at the bottom-right corner
M1	$-1.797421 - 1.623831i$	$-2.159776 - 1.1121433i$
M2	$-2.002861 - 1.830731i$	$-2.286023 - 0.6074848i$
M3	$-2.004432 - 1.834939i$	$-2.281396 - 0.6023984i$
M4	$-2.004452 - 1.834918i$	$-2.281486 - 0.6025412i$

TABLE 4.7
Primary eddy and top left eddies.

$\mathrm{Re} = 1000$	PE	TL1	TL2
φ	-0.1189366	–	–
x	0.5307901	–	–
y	0.5652406	–	–
$\mathrm{Re} = 2500$	PE	TL1	TL2
φ	-0.1214690	0.0003434479	–
x	0.5197769	0.04300225	–
y	0.5439244	0.8893601	–
$\mathrm{Re} = 5000$	PE	TL1	TL2
φ	-0.1222259	0.001447836	–
x	0.5150937	0.06335428	–
y	0.5352620	0.9092566	–
$\mathrm{Re} = 7500$	PE	TL1	TL2
φ	-0.1223867	0.002134683	–
x	0.5130967	0.06665739	–
y	0.5318922	0.9114901	–
$\mathrm{Re} = 10000$	PE	TL1	TL2
φ	-0.1223999	0.002630798	–
x	0.5119015	0.07047748	–
y	0.5300262	0.9105943	–
$\mathrm{Re} = 12500$	PE	TL1	TL2
φ	-0.1223661	0.003006600	$-1.716189 \cdot 10^{-6}$
x	0.5110722	0.07406084	0.007084863
y	0.5288052	0.9104110	0.8305045
$\mathrm{Re} = 20000$	PE	TL1	TL2
φ	-0.1222021	0.003758370	-0.00007281184
x	0.5095672	0.08031964	0.02460025
y	0.5267332	0.9116668	0.8193362
$\mathrm{Re} = 25000$	PE	TL1	TL2
φ	-0.1220905	0.004104536	-0.0001314353
x	0.5089511	0.08268173	0.02912220
y	0.5259381	0.9122620	0.8152559

TABLE 4.8
First four secondary bottom-left eddies.

Re = 1000	BL1	BL2	BL3	BL4
φ	0.0002334529	$-6.398554 \cdot 10^{-9}$	$1.764264 \cdot 10^{-13}$	$-4.864580 \cdot 10^{-18}$
x	0.08327318	0.004842696	0.0002923789	0.00001764782
y	0.07809572	0.004845241	0.0002923791	0.00001764782
Re = 2500	BL1	BL2	BL3	BL4
φ	0.0009311474	$-2.811158 \cdot 10^{-8}$	$7.751069 \cdot 10^{-13}$	$-2.137191 \cdot 10^{-17}$
x	0.08424181	0.006129716	0.0003708612	0.00002238491
y	0.1110061	0.006158831	0.0003708595	0.00002238491
Re = 5000	BL1	BL2	BL3	BL4
φ	0.001376674	$-6.667657 \cdot 10^{-8}$	$1.838104 \cdot 10^{-12}$	$-5.068178 \cdot 10^{-17}$
x	0.07285071	0.007849997	0.0004781458	0.00002886038
y	0.1370629	0.007996012	0.0004781386	0.00002886038
Re = 7500	BL1	BL2	BL3	BL4
φ	0.001536609	$-2.044008 \cdot 10^{-7}$	$5.623333 \cdot 10^{-12}$	$-1.550514 \cdot 10^{-16}$
x	0.06425712	0.01106468	0.0006880910	0.00004153326
y	0.1529439	0.01177737	0.0006881077	0.00004153326
Re = 10000	BL1	BL2	BL3	BL4
φ	0.001619610	$-1.133848 \cdot 10^{-6}$	$3.077281 \cdot 10^{-11}$	$-8.484942 \cdot 10^{-16}$
x	0.05881864	0.01720079	0.001119863	0.00006760397
y	0.1622506	0.02033695	0.001120185	0.00006760397
Re = 12500	BL1	BL2	BL3	BL4
φ	0.001667856	$-6.789915 \cdot 10^{-6}$	$1.828845 \cdot 10^{-10}$	$-5.042648 \cdot 10^{-15}$
x	0.05552998	0.02678565	0.001769764	0.0001068540
y	0.1675260	0.03269075	0.001770830	0.0001068540
Re = 20000	BL1	BL2	BL3	BL4
φ	0.001640946	-0.00008582766	$2.444284 \cdot 10^{-9}$	$-6.739573 \cdot 10^{-14}$
x	0.04796285	0.05946492	0.003474268	0.0002094783
y	0.1831827	0.05454304	0.003466804	0.0002094795
Re = 25000	BL1	BL2	BL3	BL4
φ	0.001579721	-0.0001442676	$4.490552 \cdot 10^{-9}$	$-1.238149 \cdot 10^{-13}$
x	0.04370035	0.06897488	0.004061093	0.0002443891
y	0.1936400	0.05974694	0.004036903	0.0002443913

the first time in the present work. The results of the computations on the finest mesh (4th refinement) are presented in Tables 4.7–4.10. Table 4.7 presents the results for the primary eddy (PE) and the top-left eddies (TL1 and TL2). Intensity and position of the first four secondary bottom-left eddies (BL1, BL2, BL3, and BL4) and the first four secondary bottom-right eddies (BL1, BR2, BR3, and BR4) are given in Tables 4.8 and 4.9, respectively. Table 4.10 presents the subsequent secondary bottom-left and bottom-right eddies (BLk, BRk for $k = 5, 6, 7, \ldots$). As was mentioned earlier, the solution for Re = 20000 and Re = 25000 might not be stable; the results for Re = 20000 and Re = 25000 are presented to demonstrate the capability of the present method to compute infinite series of eddies for high Reynolds numbers.

The secondary eddies starting from the fifth one (Table 4.10) are computed for the first time in the present work. The relative difference between computations of these eddies on the meshes M3 and M4 was found to be relatively small (from 10^{-7} for Re = 1000, to 0.02 for Re = 12500, to 0.2 for Re = 25000). This suggests that the present results are very accurate for small and moderate Reynolds numbers, relatively accurate for high Reynolds numbers, and have the correct order of magnitude for very high Reynolds numbers.

TABLE 4.9
First four secondary bottom-right eddies.

Re = 1000	BR1	BR2	BR3	BR4
φ	0.001729717	$-5.039380 \cdot 10^{-8}$	$1.389493 \cdot 10^{-12}$	$-3.831230 \cdot 10^{-17}$
x	0.8640401	0.9923249	0.9995375	0.9999721
y	0.1118062	0.007650979	0.0004625364	0.00002791836
Re = 2500	BR1	BR2	BR3	BR4
φ	0.002662432	$-1.226678 \cdot 10^{-7}$	$3.381770 \cdot 10^{-12}$	$-9.324506 \cdot 10^{-17}$
x	0.8344014	0.9904594	0.9994289	0.9999655
y	0.09075692	0.009384439	0.0005710737	0.00003446937
Re = 5000	BR1	BR2	BR3	BR4
φ	0.003073769	$-1.428840 \cdot 10^{-6}$	$3.895301 \cdot 10^{-11}$	$-1.074046 \cdot 10^{-15}$
x	0.8046254	0.9783735	0.9987908	0.9999270
y	0.07274733	0.01877724	0.001208945	0.00007297819
Re = 7500	BR1	BR2	BR3	BR4
φ	0.003227365	-0.00003281339	$8.935022 \cdot 10^{-10}$	$-2.463641 \cdot 10^{-14}$
x	0.7903051	0.9515559	0.9972834	0.9998361
y	0.06516917	0.04215257	0.002715411	0.0001639360
Re = 10000	BR1	BR2	BR3	BR4
φ	0.003191794	-0.0001405298	$3.958172 \cdot 10^{-9}$	$-1.091380 \cdot 10^{-13}$
x	0.7750779	0.9351074	0.9959780	0.9997570
y	0.05927927	0.06783312	0.004028554	0.0002429611
Re = 12500	BR1	BR2	BR3	BR4
φ	0.003100299	-0.0002559075	$7.759087 \cdot 10^{-9}$	$-2.139370 \cdot 10^{-13}$
x	0.7598890	0.9273684	0.9952262	0.9997111
y	0.05417034	0.08114478	0.004798437	0.0002888828
Re = 20000	BR1	BR2	BR3	BR4
φ	0.002804680	-0.0004631796	$2.751310 \cdot 10^{-8}$	$-7.583167 \cdot 10^{-13}$
x	0.7229077	0.9304323	0.9931888	0.9995836
y	0.04314560	0.1049409	0.006989903	0.0004163614
Re = 25000	BR1	BR2	BR3	BR4
φ	0.002626643	-0.0005697908	$9.317143 \cdot 10^{-8}$	$-2.560741 \cdot 10^{-12}$
x	0.7039900	0.9326059	0.9904202	0.9994010
y	0.03808287	0.1169556	0.01031843	0.0005989798

4.2. Corner subdomain shrinking factor. In order to find an optimal shrinking factor of the corner subdomain, computation of the corner eddies for the lid-driven cavity problem with shrinking factors of $2^{3/2} \approx 2.8$, $2^2 = 4$, and $2^{5/2} \approx 5.7$ was done. Figure 4.3 shows the relative error of computation of the fourth left corner eddy (BL4) plotted against the number of degrees of freedom (DOF). Computations were done on the meshes M0, M1, M2, and M3. As earlier, the error was approximately computed as the difference with the solution on the mesh M4. The continuous line on graph 4.3 corresponds to the shrinking factor of 4, and the round and square markers correspond to the shrinking factors of $2^{3/2}$ and $2^{5/2}$, respectively.

As can be seen from the graph, the error for the shrinking factor of $2^{3/2}$ is insignificantly less for DOF ≈ 2000 and is greater for the solution with more degrees of freedom. The error for the shrinking factor of $2^{5/2}$ is close to the error for the factor of 4 for the same mesh refinement, which makes the shrinking factor of $2^{5/2}$ less preferable because of larger degrees of freedom for the same mesh refinement. Thus, the solution for the shrinking factor of 4 generally performs better than for the factors of $2^{3/2}$ and $2^{5/2}$, since, generally, it has the smaller error for the same number of degrees of freedom. Therefore, we can conclude that the shrinking factor of 4 is close to the optimal value.

TABLE 4.10

kth secondary bottom-left and bottom-right eddy ($k = 5, 6, 7, \ldots$). Here $\Phi_\lambda \approx -0.000027572858$ and $R_\lambda \approx 0.060359400$.

Re = 1000	BLk	BRk
φ	$(1.341304 \cdot 10^{-22})\,\Phi_\lambda^{k-5}$	$(1.056380 \cdot 10^{-21})\,\Phi_\lambda^{k-5}$
x	$(1.065212 \cdot 10^{-6})\,R_\lambda^{k-5}$	$1 - (1.685136 \cdot 10^{-6})\,R_\lambda^{k-5}$
y	$(1.065212 \cdot 10^{-6})\,R_\lambda^{k-5}$	$(1.685136 \cdot 10^{-6})\,R_\lambda^{k-5}$
Re = 2500	**BLk**	**BRk**
φ	$(5.892847 \cdot 10^{-22})\,\Phi_\lambda^{k-5}$	$(2.571033 \cdot 10^{-21})\,\Phi_\lambda^{k-5}$
x	$(1.351140 \cdot 10^{-6})\,R_\lambda^{k-5}$	$1 - (2.080551 \cdot 10^{-6})\,R_\lambda^{k-5}$
y	$(1.351140 \cdot 10^{-6})\,R_\lambda^{k-5}$	$(2.080551 \cdot 10^{-6})\,R_\lambda^{k-5}$
Re = 5000	**BLk**	**BRk**
φ	$(1.397442 \cdot 10^{-21})\,\Phi_\lambda^{k-5}$	$(2.961451 \cdot 10^{-20})\,\Phi_\lambda^{k-5}$
x	$(1.741995 \cdot 10^{-6})\,R_\lambda^{k-5}$	$1 - (4.404920 \cdot 10^{-6})\,R_\lambda^{k-5}$
y	$(1.741995 \cdot 10^{-6})\,R_\lambda^{k-5}$	$(4.404920 \cdot 10^{-6})\,R_\lambda^{k-5}$
Re = 7500	**BLk**	**BRk**
φ	$(4.275209 \cdot 10^{-21})\,\Phi_\lambda^{k-5}$	$(6.792962 \cdot 10^{-19})\,\Phi_\lambda^{k-5}$
x	$(2.506923 \cdot 10^{-6})\,R_\lambda^{k-5}$	$1 - (9.895086 \cdot 10^{-6})\,R_\lambda^{k-5}$
y	$(2.506923 \cdot 10^{-6})\,R_\lambda^{k-5}$	$(9.895086 \cdot 10^{-6})\,R_\lambda^{k-5}$
Re = 10000	**BLk**	**BRk**
φ	$(2.339541 \cdot 10^{-20})\,\Phi_\lambda^{k-5}$	$(3.009246 \cdot 10^{-18})\,\Phi_\lambda^{k-5}$
x	$(4.080535 \cdot 10^{-6})\,R_\lambda^{k-5}$	$1 - (0.00001466503)\,R_\lambda^{k-5}$
y	$(4.080535 \cdot 10^{-6})\,R_\lambda^{k-5}$	$(0.00001466503)\,R_\lambda^{k-5}$
Re = 12500	**BLk**	**BRk**
φ	$(1.390402 \cdot 10^{-19})\,\Phi_\lambda^{k-5}$	$(5.898856 \cdot 10^{-18})\,\Phi_\lambda^{k-5}$
x	$(6.449646 \cdot 10^{-6})\,R_\lambda^{k-5}$	$1 - (0.00001743686)\,R_\lambda^{k-5}$
y	$(6.449646 \cdot 10^{-6})\,R_\lambda^{k-5}$	$(0.00001743686)\,R_\lambda^{k-5}$
Re = 20000	**BLk**	**BRk**
φ	$(1.858293 \cdot 10^{-18})\,\Phi_\lambda^{k-5}$	$(2.090896 \cdot 10^{-17})\,\Phi_\lambda^{k-5}$
x	$(0.00001264402)\,R_\lambda^{k-5}$	$1 - (0.00002513155)\,R_\lambda^{k-5}$
y	$(0.00001264402)\,R_\lambda^{k-5}$	$(0.00002513155)\,R_\lambda^{k-5}$
Re = 25000	**BLk**	**BRk**
φ	$(3.413930 \cdot 10^{-18})\,\Phi_\lambda^{k-5}$	$(7.060695 \cdot 10^{-17})\,\Phi_\lambda^{k-5}$
x	$(0.00001475125)\,R_\lambda^{k-5}$	$1 - (0.00003615330)\,R_\lambda^{k-5}$
y	$(0.00001475125)\,R_\lambda^{k-5}$	$(0.00003615330)\,R_\lambda^{k-5}$

4.3. Backward-facing step problem. The problem of the flow around a backward-facing step is another benchmark problem used for testing numerical methods. Unlike the lid-driven cavity problem, there are few works that would compute several corner eddies for the backward-facing step problem. Also, because there are more parameters to choose in the backward-facing step problem (i.e., expansion ratio and two channel lengths), different authors perform computations using different

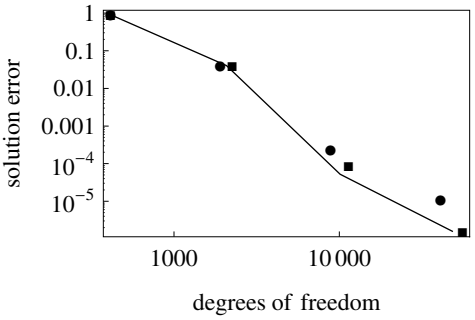

FIG. 4.3. *Estimated relative error of computation of BLA for different shrinking factors.*

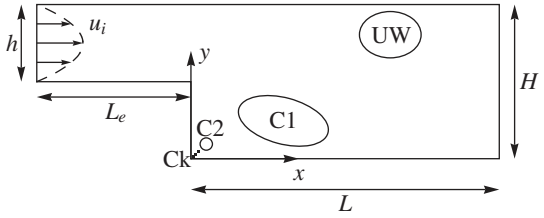

FIG. 4.4. *Schematic structure of the domain and the eddies for the backward-facing step flow.*

parameters. This makes comparison between different works for this problem more difficult than for the lid-driven cavity problem. Therefore, instead of comprehensive comparison of computation of series of corner eddies for this problem, we just compute the backward-facing step flow for one choice of parameters and compare our results with one of the works available in the literature (namely, with [23]).

The schematic structure of the domain and the eddies for the backward-facing step flow is shown in Figure 4.4. There is one upper wall eddy (UW) and a series of corner eddies (C1, C2, ..., Ck, ...). The first corner eddy is sometimes referred in the literature as the "lower wall eddy".

We chose the parameters of the problem in accordance with the first computational example of [23]. The domain sizes and Reynolds number in the computed example are chosen as follows: $L = 20$, $L_e = 3$, $H = 1$, $h = 0.5$, $\mathrm{Re} = 1000$. The standard parabolic velocity with a maximum value of 1 is prescribed at the inlet (at $x = -L_e$). At the position of the outlet $x = L$, contrary to the conventional outflow conditions, the velocity is set to be equal to velocity at $x \to \infty$. We found that these boundary conditions produce the same results as the other boundary conditions tried in the literature, but are easier to implement. With these boundary conditions, the problem takes the form

$$\begin{cases} \Delta\Delta\varphi + \mathrm{Re}\left(\dfrac{\partial\Delta\varphi}{\partial x}\dfrac{\partial\varphi}{\partial y} - \dfrac{\partial\Delta\varphi}{\partial y}\dfrac{\partial\varphi}{\partial x}\right) = 0, \\ \varphi|_{\partial\Omega} = \varphi_0, \\ \left.\dfrac{\partial\varphi}{\partial n}\right|_{\partial\Omega} = 0, \end{cases}$$

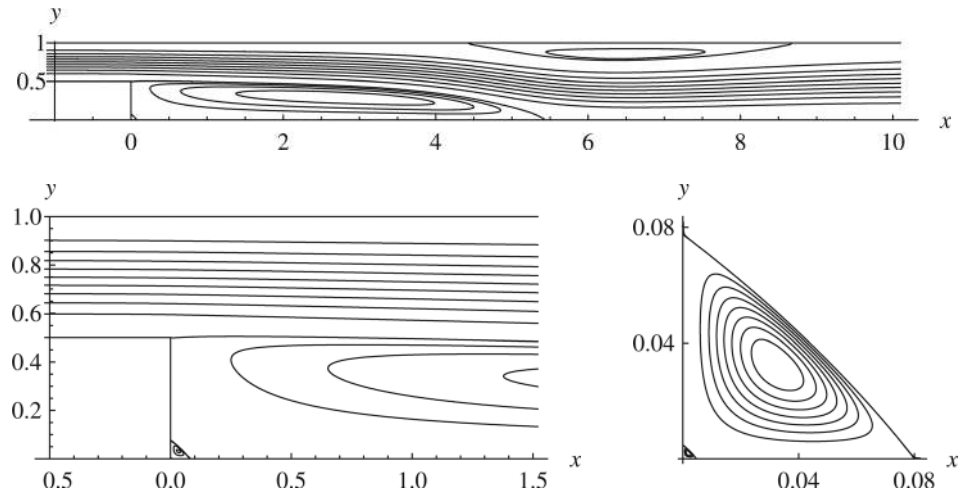

FIG. 4.5. *Streamlines of the backward-facing step flow.*

where

$$\varphi_0(x,y) = \begin{cases} \dfrac{2(3H-h-2y)(y-h)^2}{3(H-h)^2}, & \text{for } x = -L_e, \\ \dfrac{1}{3}(3-2y)y^2, & \text{for } x = L, \\ 0, & \text{for } -L_e < x < L. \end{cases}$$

There were two insignificant differences in choice of parameters between our work and [23]. First, the value of Reynolds number in [23] was 500 due to the different way of defining it. And second, the outlet boundary conditions in [23] were such that the normal derivatives of velocity were zero at the outlet. However, as was stated in [23], with the chosen outlet boundary conditions and the channel length L, their results were "channel-length-independent". For our case, we found out that our results are also independent of the channel length: The relative difference in intensity of eddies between the flows with $L = 20$ and $L = 25$ is less than 10^{-12}. Therefore, it is valid to compare these two examples.

The graphs with streamlines of the backward-facing step flow are presented in Figure 4.5. The upper graph has the eddies UW and C1, the lower left graph contains C1 and C2, and the lower right graph shows C2 and C3.

The backward-facing step problem was computed on three different meshes denoted as M1, M2, and M3. The mesh M1 is shown in Figure 4.6, where the bold lines correspond to the boundaries of near-corner subdomains. Near the 90-degree corner the mesh is similar to the near-corner mesh for the lid-driven cavity problem. The mesh at the backward-facing 270-degree corner is constructed by splitting the corner into three 90-degree angles and combining the meshes for those 90-degree angles, as shown in Figure 4.6. The details of the meshes used are presented in Table 4.11, where the table columns are the same as in Table 4.1. Also, some details of the discretization of [23] are presented in Table 4.1.

Intensity (φ) and position (x, y) of the upper wall eddy UW and the corner eddies C1, C2, C3, and Ck ($k = 4, 5, \ldots$) are presented together with the results of [23] in Table 4.12. As can be seen from the table, the absolute difference in intensity

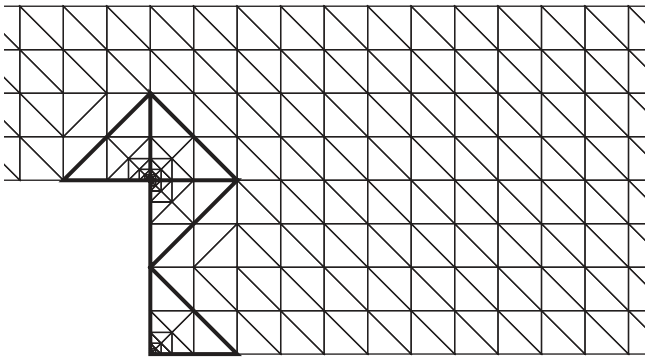

FIG. 4.6. *Mesh M1 used for the backward-facing step problem.*

TABLE 4.11
Parameters of meshes used.

Mesh	Triangles	DOF	Reduced DOF	Corner triangle size (OG)	Near-corner radial subdivisions(m)	Near-corner angular subdivisions(n)
present (M1)	2852	14268	11786	0.0020	6	1
present (M2)	11524	54790	49720	0.00049	17	3
present (M3)	46596	215666	205344	0.00012	43	7
[23]		23414	17564			

TABLE 4.12
Results of computation of the backward-facing corner problem.

Work (mesh)		UW	C1	C2	C3
present (M1)	φ	0.3358312568	-0.022261362	$5.00806 \cdot 10^{-7}$	$-1.383685 \cdot 10^{-11}$
	x	6.463736747	2.77208792	0.03233880	0.001953041
	y	0.847563780	0.29352617	0.03246756	0.001953396
present (M2)	φ	0.3358309224	-0.022261464	$4.92964 \cdot 10^{-7}$	$-1.359039 \cdot 10^{-11}$
	x	6.463424442	2.77233160	0.03241694	0.001950378
	y	0.847566677	0.29352462	0.03221787	0.001950591
present (M3)	φ	0.3358309259	-0.022261475	$4.92906 \cdot 10^{-7}$	$-1.359057 \cdot 10^{-11}$
	x	6.463423960	2.77233327	0.03241492	0.001950368
	y	0.847566601	0.29352457	0.03221771	0.001950582
[23]	φ	0.3357	0.02215		
	x	6.47	2.76	not resolved	not resolved
	y	0.849	0.278		

Work (mesh)		Ck
present (M1)	φ	$(3.8887 \cdot 10^{-16})\, \Phi_\lambda^{k-4}$
	x	$0.000118619\, R_\lambda^{k-4}$
	y	$0.000118619\, R_\lambda^{k-4}$
present (M2)	φ	$(3.7459 \cdot 10^{-16})\, \Phi_\lambda^{k-4}$
	x	$0.000117718\, R_\lambda^{k-4}$
	y	$0.000117718\, R_\lambda^{k-4}$
present (M3)	φ	$(3.7473 \cdot 10^{-16})\, \Phi_\lambda^{k-4}$
	x	$0.000117729\, R_\lambda^{k-4}$
	y	$0.000117729\, R_\lambda^{k-4}$
[23]	φ	
	x	not resolved
	y	

of the eddies between the present solution and [23] is of the order of 10^{-4}. The absolute difference in intensity between the present results on the meshes M2 and M3 is $1.1 \cdot 10^{-8}$. The relative difference in intensity of the eddies Ck ($k \geq 4$) is $3.7 \cdot 10^{-4}$. Thus, we can conclude that the proposed method efficiently computes the solution of the backward-facing corner problem, and allows one to compute all the eddies present in the flow relatively accurately.

5. Conclusion. The method for computing the infinite series of eddies in viscous fluid flows in domains with corners was proposed. The method is based on Argyris finite element discretization for the stream function formulation of the Navier–Stokes equations, exponential mesh refinement near corners, and asymptotics of the flow near corners. The method was applied to two benchmark problems: The lid-driven cavity problem and the backward-facing step problem. The results of computations demonstrate high accuracy of the present method, show that the method can accurately compute the infinite series of eddies, and indicate that the relative error of finding eddies' intensity and position decreases uniformly as the mesh is refined (i.e. the error of finding intensity and position of different eddies does not depend on their size). The comparison with the results available in the literature shows that the present method produces solutions of the same or better accuracy than the existing methods.

Acknowledgments. The authors are thankful to Prof. Bruneau and Prof. Rannacher for valuable comments on the present work. The authors would also like to thank the referees for their suggestions on improving the article.

REFERENCES

[1] T. Apel and F. Milde, *Comparison of several mesh refinement strategies near edges*, Comm. Numer. Methods Engrg., 12 (1996), pp. 373–381.

[2] F. Assous, P. Ciarlet, Jr., and J. Segré, *Numerical solution to the time-dependent Maxwell equations in two-dimensional singular domains: The singular complement method*, J. Comput. Phys., 161 (2000), pp. 218–249.

[3] I. Babuška, R. B. Kellogg, and J. Pitkäranta, *Direct and inverse error estimates for finite elements with mesh refinements*, Numer. Math., 33 (1979), pp. 447–471.

[4] E. Barragy and G. F. Carey, *Stream function-vorticity driven cavity solution using p finite elements*, Comput. & Fluids, 26 (1997), pp. 453–468.

[5] H. Blum, *Der Einfluß von Eckensingularitäten bei der numerischen Behandlung der biharmonischen Gleichung*, Bonner Mathematische Schriften [Bonn Mathematical Publications], 140, Universität Bonn Mathematisches Institut, Bonn, 1981. Dissertation, Rheinische Friedrich-Wilhelms-Universität, Bonn, 1981.

[6] H. Blum, *A simple and accurate method for the determination of stress intensity factors and solutions for problems on domains with corners*, The Mathematics of Finite Elements and Applications IV, MAFELAP 1981, Proc. Conf., Uxbridge/Middlesex, 1981, pp. 57–64.

[7] H. Blum and M. Dobrowolski, *On finite element methods for elliptic equations on domains with corners*, Computing, 28 (1982), pp. 53–63.

[8] H. Blum and R. Rannacher, *On the boundary value problem of the biharmonic operator on domains with angular corners*, Math. Methods Appl. Sci., 2 (1980), pp. 556–581.

[9] O. Botella and R. Peyret, *Benchmark spectral results on the lid-driven cavity flow*, Comput. & Fluids, 27 (1998), pp. 421–433.

[10] M. Bourlard, M. Dauge, M.-S. Lubuma, and S. Nicaise, *Coefficients of the singularities for elliptic boundary value problems on domains with conical points. III. Finite element methods on polygonal domains*, SIAM J. Numer. Anal., 29 (1992), pp. 136–155.

[11] S. C. Brenner, *Overcoming corner singularities using multigrid methods*, SIAM J. Numer. Anal., 35 (1998), pp. 1883–1892.

[12] C. H. Bruneau and M. Saad, *The 2D lid-driven cavity problem revisited*, Comput. & Fluids, 35 (2006), pp. 326–348.

[13] C. H. Bruneau and C. Jouron, *An efficient scheme for solving steady incompressible Navier-Stokes equations*, J. Comput. Phys., 89 (1990), pp. 389–413.

[14] P. Burda, J. Novotny, and J. Sistek, *Precise FEM solution of a corner singularity using adjusted mesh*, Internat. J. Numer. Methods Fluids, 47 (2005), pp. 1285–1292.
[15] Z. Chen, *Finite Element Methods and Their Applications*, Springer, New York, 2005.
[16] T. A. Davis, *Algorithm 832: Umfpack v4.3—an unsymmetric-pattern multifrontal method*, ACM Trans. Math. Software, 30 (2004), pp. 196–199.
[17] T. A. Davis, *A column pre-ordering strategy for the unsymmetric-pattern multifrontal method*, ACM Trans. Math. Software, 30 (2004), pp. 165–195.
[18] E. Erturk, T. C. Corke, and C. Gokcol, *Numerical solutions of 2-d steady incompressible driven cavity flow at high reynolds numbers*, Internat. J. Numer. Methods Fluids, 48 (2005), pp. 747–774.
[19] G. J. Fix, S. Gulati, and G. I. Wakoff, *On the use of singular functions with finite element approximations*, J. Comput. Phys., 13 (1973), pp. 209–228.
[20] U. Ghia, K. N. Ghia, and C. T. Shin, *High-re solutions for incompressible-flow using the Navier-Stokes equations and a multigrid method*, J. Comput. Phys., 48 (1982), pp. 387–411.
[21] D. Givoli and L. Rivkin, *The DtN finite element method for elastic domains with cracks and re-entrant corners*, Comput. & Structures, 49 (1993), pp. 633–642.
[22] O. Goyon, *High-reynolds number solutions of Navier-Stokes equations using incremental unknowns*, Comput. Methods Appl. Mech. Engrg., 130 (1996), pp. 319–335.
[23] M. M. Grigoriev and A. V. Fafurin, *A boundary element method for steady viscous fluid flow using penalty function formulation*, Internat. J. Numer. Methods Fluids, 25 (1997), pp. 907–929.
[24] M. M. Gupta, R. P. Manohar, and B. Noble, *Nature of viscous flows near sharp corners*, Comput. & Fluids, 9 (1981), pp. 379–388.
[25] K. Gustafson and R. Leben, *Multigrid calculation of subvortices*, Appl. Math. Comput., 19 (1986), pp. 89–102.
[26] T. Hawa and Z. Rusak, *Numerical-asymptotic expansion matching for computing a viscous flow around a sharp expansion corner*, Theoretical and Computational Fluid Dynamics, 15 (2002), pp. 265–281.
[27] V. A. Kondrat′ev, *Boundary value problems for elliptic equations in domains with conical or angular points*, Trans. Moscow Math. Soc., 16 (1967), pp. 227–313.
[28] H. K. Moffat, *Viscous and resistive eddies near a sharp corner*, J. Fluid Mech., 18 (1964), pp. 1–18.
[29] H. Nishida and N. Satofuka, *Higher-order solutions of square driven cavity flow using a variable-order multigrid method*, Internat. J. Numer. Methods Engrg., 34 (1992), pp. 637–653.
[30] L. A. Oganesyan and L. A. Rukhovets, *Variational-difference methods for the solution of elliptic equations*, Izv. Akad. Nauk Armyanskoi SSR, Jerevan, 1979.
[31] G. Raugel, *Résolution numérique par une méthode d'éléments finis du problème de Dirichlet pour le laplacien dans un polygone*, C. R. Math. Acad. Sci. Paris Sér. A-B, 286 (1978), pp. A791–A794.
[32] H.-G. Roos, M. Stynes, and L. Tobiska, *Numerical methods for singularly perturbed differential equations*, vol. 24 of Springer Series in Computational Mathematics, Springer-Verlag, Berlin, 1996. Convection-diffusion and flow problems.
[33] A. Seweryn, *Modeling of singular stress fields using finite element method*, Internat. J. Solids Structures, 39 (2002), pp. 4787–4804.
[34] J. M. Shi, M. Breuer, and F. Durst, *A combined analytical-numerical method for treating comer singularities in viscous flow predictions*, Internat. J. Numer. Methods Fluids, 45 (2004), pp. 659–688.
[35] G. Strang and G. J. Fix, *An Analysis of the Finite Element Method*, Prentice-Hall Inc., Englewood Cliffs, NJ, 1973. Prentice-Hall Series in Automatic Computation.